PAPER

Fine-tuning near-boundary swimming equilibria using asymmetric kinematics

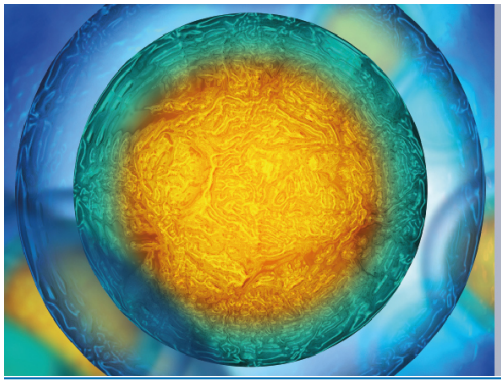

IOP Publishing Bioinspir. Biomim. 18 (2023) 016011 https://doi.org/10.1088/1748-3190/aca131

Bioinspiration & Biomimetics

PAPER

RECEIVED
8 July 2022

REVISED
14 October 2022

ACCEPTED FOR PUBLICATION
8 November 2022

PUBLISHED
29 November 2022

Fine-tuning near-boundary swimming equilibria using asymmetric kinematics

Leo Liu[1], **Qiang Zhong**[2], **Tianjun Han**[3], **Keith W Moored**[3] **and Daniel B Quinn**[4,*]

[1] Mechanical & Aerospace Engineering, University of Virginia, Charlottesville, VA 22904, United States of America
[2] Mechanical Engineering, Iowa State University, Ames, IA 50011, United States of America
[3] Mechanical Engineering and Mechanics, Lehigh University, Bethlehem, PA 18015, United States of America
[4] Mechanical & Aerospace Engineering, Electrical & Computer Engineering, University of Virginia, Charlottesville, VA 22904, United States of America
[*] Author to whom any correspondence should be addressed.

E-mail: danquinn@virginia.edu

Keywords: asymmetric kinematics, ground effect, pitching hydrofoil, spacial asymmetry, temporal asymmetry, equilibrium altitude, dynamic boundary interaction

Abstract

When swimming near a solid planar boundary, bio-inspired propulsors can naturally equilibrate to certain distances from that boundary. How these equilibria are affected by asymmetric swimming kinematics is unknown. We present here a study of near-boundary pitching hydrofoils based on water channel experiments and potential flow simulations. We found that asymmetric pitch kinematics do affect near-boundary equilibria, resulting in the equilibria shifting either closer to or away from the planar boundary. The magnitude of the shift depends on whether the pitch kinematics have spatial asymmetry (e.g. a bias angle, θ_0) or temporal asymmetry (e.g. a stroke-speed ratio, τ). Swimming at stable equilibrium requires less active control, while shifting the equilibrium closer to the boundary can result in higher thrust with no measurable change in propulsive efficiency. Our work reveals how asymmetric kinematics could be used to fine-tune a hydrofoil's interaction with a nearby boundary, and it offers a starting point for understanding how fish and birds use asymmetries to swim near substrates, water surfaces, and sidewalls.

1. Introduction

Swimming and flying near planar boundaries can lead to propulsive benefits. In nature, ground effect lowers the cost of transport and increases range for animals such as brown pelicans [15, 31], herring gulls [3], black skimmers [5, 40], bats [17], mandarin fish [6], and flying fish [27]. These benefits stem from 'steady ground effect', where fixed wings/fins experience a boost in lift near a solid boundary. Wings/fins that oscillate near a boundary experience 'unsteady ground effect'. Unsteady ground effect can cause near-boundary rigid oscillating hydrofoils [23, 24, 29, 44], flexible oscillating hydrofoils [30], and flexible undulating hydrofoils [12] to experience thrust benefits with little to no cost in efficiency. Low-Reynolds-number simulations have produced similar trends [9, 28, 36, 42]. There are some exceptions, such as a flexible undulating fin that experienced no change in self-propelled speed near the ground [7], but in general, swimming near the ground leads to higher thrust.

Solid planar boundaries, such as riverbeds or the ocean floor, also create stable equilibria for oscillating hydrofoils. Oscillating too close to the ground causes a net force propelling the hydrofoil away from the ground; oscillating too far from the ground causes a net force attracting the hydrofoil towards the ground (figure 1). At some intermediate altitude, the net lateral force is zero [21], forming a stable 'equilibrium altitude', which a hydrofoil will naturally converge to without external disturbances. Shifting these equilibrium altitudes may require alterations in swimming kinematics, but given the thrust benefits and/or possible energy savings, that extra complexity may be worth the cost.

Previous studies of unsteady ground effect mainly focused on symmetrical and sinusoidal pitch motions [41]. While sinusoidal gaits are often assumed in studies of bio-inspired propulsion, real animal gaits

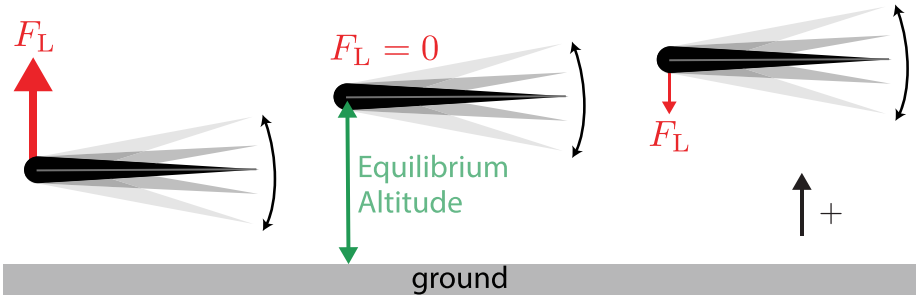

Figure 1. Schematic of a pitching hydrofoil at different altitudes near the ground (planar boundary). The lift force (F_L) of a pitching hydrofoil switches from positive to negative as the foil moves away from the planar boundary. The proximity at which $F_L = 0$ is the 'equilibrium altitude'.

can be asymmetric and complex [22]. Asymmetry in swimming/flying can be classified into two types: spatial and temporal. Spatial asymmetry is introduced by tuning the geometric angle of a fin/wing. Cownose rays, for example, use a larger upstroke than downstroke [33, 43], and pigeons tilt their lift vector to turn, much like a helicopter [34]. Temporal asymmetry is introduced by tuning the speed of a fin/wing during the stroke cycle. Dolphin tails, for example, tend to have a faster downstroke than upstroke [35, 38], and insects/bats/birds use asymmetric wingbeats to produce yaw torques [16].

Asymmetric kinematics are particularly relevant to near-boundary swimming/flying, because they could shift near-boundary equilibria and therefore lead to force/energetic benefits. How asymmetries factor into near-boundary propulsion is currently unknown. To explore this new area, we considered spatial and temporal asymmetries in the pitch oscillations of a hydrofoil near a solid boundary and set out to answer two questions: (a) Does asymmetric kinematics affect the existence and/or position of equilibrium altitudes? (b) Does asymmetric kinematics affect thrust production and efficiency? We answered these question through a combination of direct force and power measurements and potential flow simulations.

2. Methods

In order to test asymmetric pitch kinematics systematically, we employed a previously developed function for pitch angle that incorporates both spatial and temporal asymmetries [45]. The function gives pitch angle as the following function of time:

$$\theta(t) = \theta_0 + \alpha \frac{\tan^{-1}[\tau \sin(2\pi f t)/(1 - \tau\cos(2\pi f t))]}{\tan^{-1}\left(\tau/\sqrt{1-\tau^2}\right)} \quad (1)$$

where α is the pitch amplitude, f is the pitch frequency, and θ_0 and τ are constants that introduce spatial and temporal asymmetries, respectively. Our study employed one asymmetry type at a time, so when we discuss one asymmetry type, the other asymmetry type is assumed to be zero. The 'bias angle', θ_0, sets the average pitch angle within a pitch cycle (figure 2(a)). When $\theta_0 = 0$, the hydrofoil undergoes symmetric pitch motion. The 'stroke speed ratio', τ, sets the difference between upstroke and downstroke speeds (figure 2(b)). As $\tau \to 0$, pitch oscillation approaches a sinusoid; as $\tau \to -1$ or $+1$, pitch oscillation becomes a sawtooth wave. To avoid the singularity in equation (1), we used $\theta(t) = \theta_0 \sin(2\pi f t)$ for the $\tau = 0$ case, which is the limit of equation (1) as $\tau \to 0$.

To examine the response of a hydrofoil pitching asymmetrically near a solid boundary, we measured the forces and kinematics of tethered and untethered hydrofoils in a recirculating water channel. We tested a laterally-constrained hydrofoil to explore how lift (and therefore equilibrium altitude), thrust, and efficiency are affected by asymmetric kinematics. Then, we tested a laterally-unconstrained hydrofoil to examine the consistency of equilibrium altitudes and if they can be shifted dynamically due to changes in swimming kinematics. Finally, we compared our results with reduced-order simulations of laterally-unconstrained and fully-unconstrained hydrofoils.

2.1. Laterally-constrained hydrofoil experiments

In our constrained hydrofoil tests, the hydrofoil was tethered in a closed-loop water channel (Rolling Hills 1520, figure 3(a)). A surface plate was installed to reduce surface waves. The incoming flow speed, $u = 143\,\text{mm}\,\text{s}^{-1}$, was regulated by a custom circuit (Arduino Mega with a signal amplifier) and an ultrasonic flowmeter (Dynasonics Series TFXB). In order to match previous studies of unsteady ground effect [21, 44, 45], we used a hydrofoil with a 7%-thick tear-drop cross-section and a rectangular planform. The hydrofoil was printed with solid acrylonitrile butadiene styrene and had a chord and span of c = 95 mm and s = 190 mm ($\mathcal{A}$Aspect ratio = 2, figure 3(b)). Our choice of u led to a chord-based Reynolds number of 13 500, which is within the range typically seen in fish ($O(10^4)$–$O(10^5)$) [1, 7].

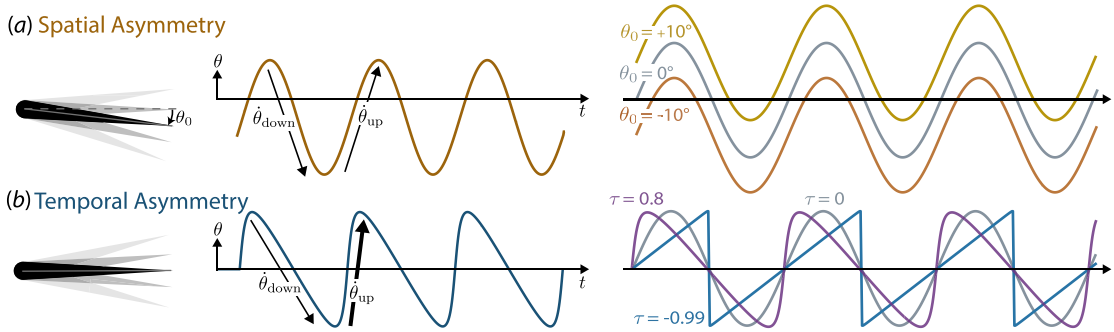

Figure 2. Types of asymmetry. (a) Spatial asymmetry is introduced by θ_0, which sets the pitch bias of the pitching hydrofoil. (b) Temporal asymmetry is introduced by τ, which sets the difference between upstroke pitch speed, $\dot{\theta}_{\text{up}}$, and downstroke pitch speed, $\dot{\theta}_{\text{down}}$. Adding temporal asymmetry does not change the total time to complete one pitch cycle.

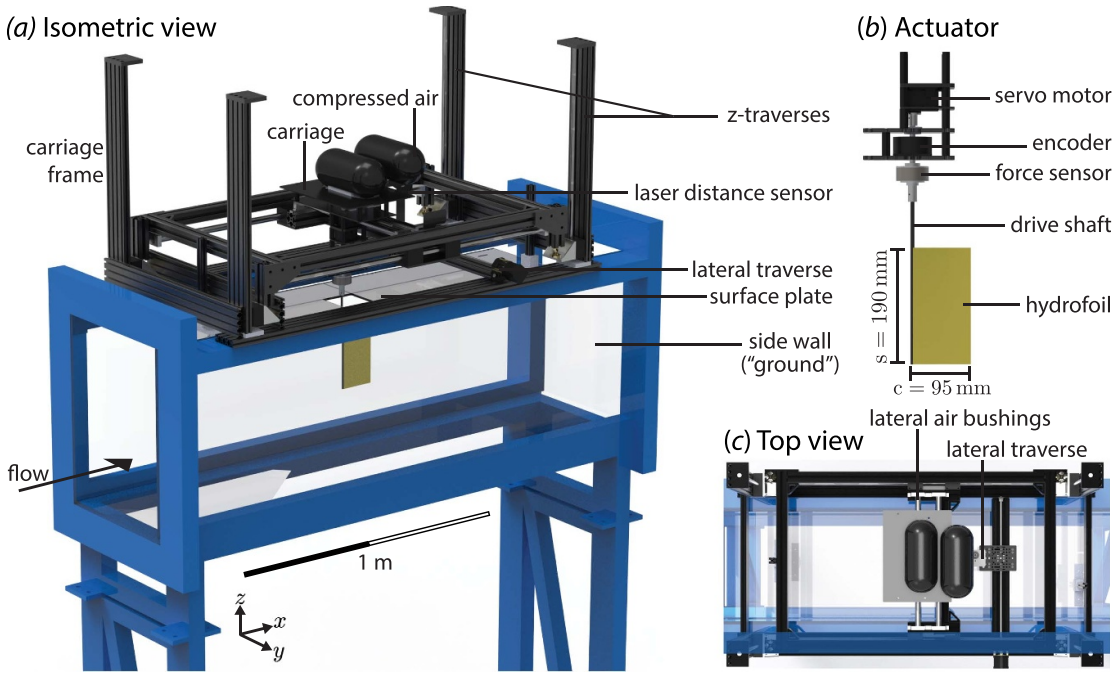

Figure 3. Experimental Apparatus. (a) Test rig mounted on top of the water channel (for both constrained and unconstrained hydrofoil experiments). Test section: 380 × 450 × 1520 mm (W × H × L). A z-traverse (stepper motor) controlled the height of each corner of the carriage frame. (b) The hydrofoil's actuation system consisted of an in-line servo motor, encoder, force sensor, and a drive shaft. (c) The sidewall of the channel served as the 'ground'. In 'constrained' tests, the rig was constrained laterally by the lateral traverse; in 'unconstrained' tests, the rig slid laterally along air bushings. The rig was constrained in the stream-wise direction in all experiments.

A high torque digital servo motor (Dynamixel MX-64) was used to pitch the hydrofoil around the carbon fiber driveshaft (6.35 mm diameter) at its leading edge with the prescribed pitch angle $\theta(t)$ (equation (1)). The pitch angle was verified by an absolute encoder (US Digital A2K 4096 CPR). Even slight asymmetries produced substantial lateral forces, so we considered narrow bands of bias angle and stroke speed ratio: θ_0 from $-1.5°$ to $+1.5°$ in increments of $0.5°$ and τ from -0.3 to $+0.3$ in increments of 0.1. For each asymmetry type, the hydrofoil was actuated with a pitch frequency of $f = 1.58$ Hz and a pitch amplitude of $\alpha = 11°$. We chose these values in order to consider biologically-inspired kinematics while keeping forces high. These inputs resulted in a Strouhal number on the upper end of those typically observed in fish: $\text{St} \equiv 2fc\sin\alpha/u = 0.4$ (reduced frequency $k \equiv fc/u = 10.5$) [11, 13, 37].

To systematically test each set of asymmetric kinematics, we actuated the hydrofoil at 15 altitudes (d) (i.e. proximities to the sidewall/'ground' of the water channel). The altitudes ranged from $d = 38.5$ mm (the lowest value before the hydrofoil came in contact with the ground) to $d = 188.5$ mm (the midpoint of the water channel). Scaled by the chord length, the normalized altitudes (d/c) ranged from around 0.4 to 2.0. An automated lateral traverse positioned the hydrofoil in between each trial.

For each altitude and motion type, we recorded forces using a six-axis force/torque sensor (ATI-Mini

40: SI-40-2) in line with the driveshaft (figure 3(b)). Data were collected over 30 pitch cycles: 5 cycles warm-up cycles, 20 active cycles, and 5 cool-down cycles. The 'net thrust' ($\overline{F_T}$) and 'net lift' ($\overline{F_L}$) were defined as the stream-wise (parallel to the ground) and lateral (perpendicular to the ground) forces averaged over the active cycles. The 'net power' ($\overline{p}$) was defined as the average product of the pitching torque and pitching velocity (as recorded by the encoder).

The thrust and power data were combined to define the propulsive efficiency: $\eta \equiv \overline{F_T}u/\overline{p}$, which represents the average fraction of the energy injected into the wake that is used for forward thrust. Because the time-averaged forces were comparable to the resolution of the sensor($(O(0.01)\,\mathrm{N})$ vs. $\pm 0.01\,\mathrm{N}$), the measured thrusts/efficiencies contained a large number of outliers. To account for this effect, we repeated each trial 10 times and omitted thrusts/efficiencies beyond 1.25 standard deviations from the average (15% of points omitted).

We chose not to employ flow visualization techniques for this study because our prior work has explored the wakes of pitching foils with symmetric and asymmetric kinematics [45] and with near-boundary kinematics [21, 44]. Our goal here was to explore near-boundary equilibrium shifting and the associated bulk performance metrics.

2.2. Laterally-unconstrained hydrofoil experiments

Laterally-unconstrained hydrofoil tests were used to validate the existence of near-boundary equilibria and to demonstrate how equilibria could be modified by asymmetry. In these tests, we removed the lateral traverse and used linear air-bushings (New Way S301901) to allow the hydrofoil to move freely in the lateral direction (figure 3(c)).

To minimize friction, we avoided any tethered contacts to the carriage. The carriage included a power source (16.8 V LiPO battery), compressed air tanks (Ninja HPA Tank—68 CI—4500 PSI) to run its air-bushings, a wireless receiver (Arduino mega 2560 with Xbee shield), a wireless transmitter (ATI F/T wireless), and a custom circuit to synchronize measurements before transmitting data to the control PC (Omen 870). Altitude d was captured by a laser distance sensor (Baumer CH-8510; ± 0.01 mm resolution). Based on observed deceleration rates with the channel drained, we estimate the friction in the bearings to be 0.0017 ± 0.0007 N.

To level the air bushing system and simulate payloads, we used four independently-controlled stepper motors to raise/lower the four corners of the carriage frame independently (figure 3(a)). These motors automatically leveled the carriage to $\pm 0.001°$ precision and reduced the effects of gravity to less than 2.5 mN [45]. We also used the leveling system to simulate a payload by tilting the carriage such that a component of its weight pulled it towards the 'ground' (sidewall). The effective mass of the wireless carriage was 4.6 kg in the lateral direction [45], leading to a simulated payload of $(4.6\,\mathrm{kg})g\sin\gamma$, where γ is the tilt angle. This payload could represent, for example, the negative buoyancy common to many rays and flatfish [4, 39].

Each unconstrained trial consisted of four stages. In Stage 1, the hydrofoil performed 30 symmetrical pitch cycles. In Stage 2, we simulated a small payload (31.5 mN) by tilting the wireless carriage 0.04° toward the 'ground'. In Stage 3, we introduced into the pitch kinematics a positive asymmetry (either spatial, $\theta_0 = 0.8°$, or temporal, $\tau = 0.25$). In Stage 4, we introduced into the pitch kinematics a negative asymmetry (either spatial, $\theta_0 = -0.5°$; or temporal, $\tau = -0.1$). Net thrust and efficiency for each stage were calculated using portions of the data in which the hydrofoil had converged to an equilibrium altitude. We ran these tests at three different initial altitudes ($d/c \approx 0.4, 0.5, 0.7$) to highlight the insensitivity of the equilibria to initial condition.

2.3. Laterally-unconstrained hydrofoil simulations

To pair with our experiments, we ran potential flow simulations of near-boundary pitching foils. Potential flow simulations assume the flow is irrotational, incompressible and inviscid [18]. The simulations provide additional evidence for trends observed in the laterally-tethered and untethered experiments. They also quantify the influence of viscous effects. In the water channel, a thin boundary layer forms on the channel wall upstream of the pitching foil. This boundary layer would not be present ahead of untethered foils swimming near boundaries in quiescent fluid, nor ahead of animals flying or swimming in ground effect. Our inviscid simulations help to quantify the importance of this discrepancy in boundary condition. Trends that are observed in both our experiments and simulations are therefore inviscid phenomena that are unrelated to the channel's boundary layer.

To model the presence of the ground, we used the method of images, where singularity elements are mirrored to satisfy no flux at the ground plane ($z = 0$). Specifically, a tear-drop hydrofoil, identical to the one used in the laterally-unconstrained experiments, was pitched at a ground distance d above the ground while an image hydrofoil was pitched 180° out-of-phase at the same ground distance d beneath the ground (figure 4). The hydrofoil was constrained in the streamwise direction but allowed to move freely in the lateral direction. Equilibrium altitudes were defined as the altitudes at which the time-averaged net lift dropped below a threshold range ($|C_L| \leqslant 0.015$). The simulations followed the same 4-stage procedure as the unconstrained hydrofoil experiments.

Following previous studies [2, 18, 19, 25], an unsteady three-dimensional boundary element method was employed. The potential flow is governed by Laplace's equation, $\nabla^2\Phi^* = 0$, where Φ^* is the

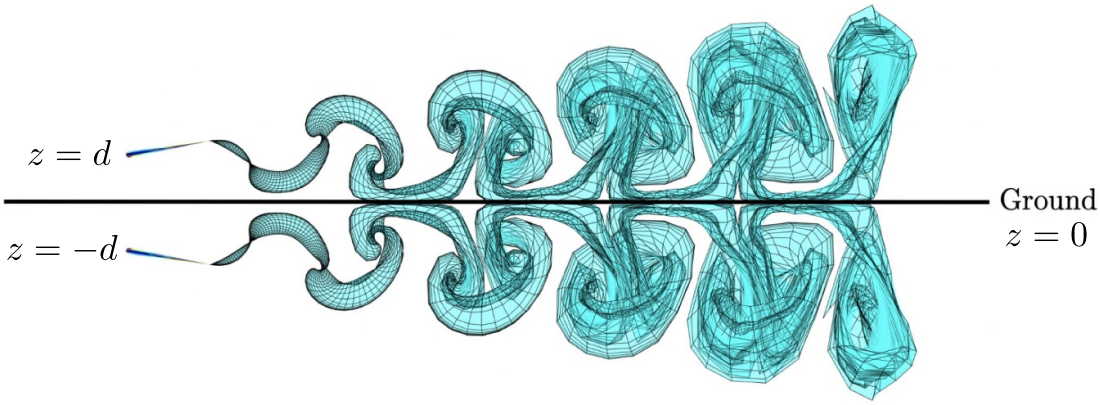

Figure 4. Illustration of the method of images in potential flow simulation.

perturbation potential in an inertial frame fixed to the undisturbed fluid. In addition, at each time step, the no-flux boundary condition must be satisfied on the surface of the propulsor S_b ($\nabla\Phi^* \cdot \boldsymbol{n} = 0$), where $\boldsymbol{n}$ is the vector normal to the hydrofoil's surface. The hydrofoil and the wake surface were then discretized by a finite number of quadrilateral boundary elements. The general solution to the potential flow problem was reduced to finding a distribution of constant-strength doublet and source boundary elements over the body and wake based on an internal Dirichlet boundary condition. Furthermore, an explicit Kutta condition was applied at the trailing edge by introducing a wake boundary element. At each time step, wake boundary elements are shed from the trailing edge, after which they advect with the local velocity calculated by the desingularized Biot–Savart law [20, 25, 46]. The forces acting on the hydrofoil were calculated by using the unsteady Bernoulli equation and integrating the resulting pressure field. Finally, the net thrust C_T is calculated by adding the profile drag coefficient $C_D = 0.047$ measured during the experiments to the simulated potential-flow-based thrust coefficient, which does not inherently include any viscous drag.

2.4. Streamwise and laterally-unconstrained hydrofoil simulations

Fully unconstrained simulations were used to demonstrate the insensitivity of near-boundary equilibria to hydrofoil surging oscillations and to draw a clear connection between laterally-unconstrained hydrofoil measurements and free-swimming performance. When the hydrofoil was unconstrained in the streamwise direction, a virtual drag force per unit span of $F'_{drag} = 0.5\, C_{drad} \rho u^2\, c$ was applied to satisfy the free-swimming condition, where there is net zero force in the streamwise direction. By iterating the drag coefficient C_{drag}, the time-averaged speed of streamwise and laterally-unconstrained simulations was matched to that of the laterally-unconstrained simulations and experiments ($u = 143\,\mathrm{mm\,s^{-1}}$) when $C_{drag} = 0.56$. This ensured that the Strouhal number and reduced frequency of the simulation hydrofoil were also the same as the conditions in Stage 1 of the laterally-unconstrained hydrofoil experiments and simulations (St = 0.4 and $k = 1$). This was necessary for a simulated foil to achieve biologically relevant Strouhal numbers since the potential flow solver does not otherwise calculate viscous drag. With the applied drag force and resultant forces from the potential flow pressure field, the equations of motion were solved in both the streamwise and lateral directions. The simulated hydrofoil had a mass of $m = 4.6$ kg to match the experiments. Results were reported as the simulated equilibrium altitudes and the free swimming speed of the hydrofoil under fully-unconstrained swimming conditions.

3. Results

3.1. Laterally constrained experiments: asymmetric kinematics shift equilibria and affect thrust

Our results for symmetric kinematics ($\theta_0 = 0°, \tau = 0$) agree with previous studies [21, 29, 44] (figure 5). The net lift was *positive* close to the ground ($d/c \lesssim 0.67$), *negative* intermediate to the ground ($0.67 \lesssim d/c \lesssim 1.4$), and *zero* far from the ground ($d/c \gg 1.4$). The result was a stable equilibrium altitude around $d/c = 0.67$. If the hydrofoil were free to move perpendicularly to the ground, it would naturally settle into this equilibrium altitude without any lateral perturbation [21].

As asymmetry was added to the pitching kinematics, the equilibrium altitude shifted. When the foil was biased away from the ground (positive θ_0), the resulting negative net force toward the ground led to a lower equilibrium altitude (figure 5(a)). The same result occurred with temporal asymmetry: with a faster pitch stroke away from the ground (positive τ), the equilibrium altitude became lower (figure 5(b)). When the asymmetries were reversed (negative θ_0 and τ), the equilibrium altitude increased. Note, however, that the negative lift caused by the ground was so

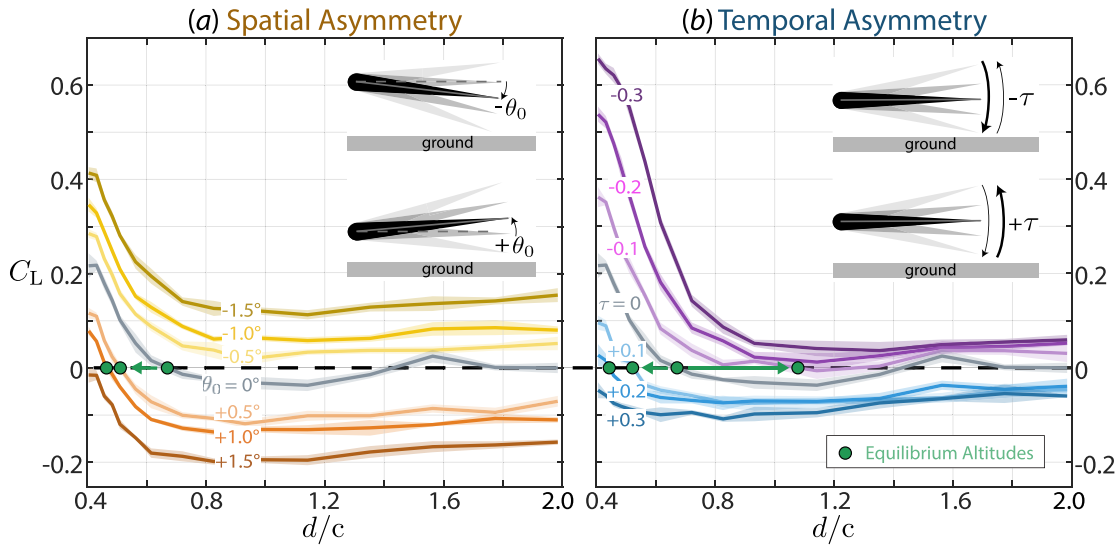

Figure 5. Lift coefficient depends on both altitude and (a) spatial and (b) temporal asymmetry parameters. Adding spatial and temporal asymmetry causes the lift coefficient ($C_{F_L} \equiv \bar{L}/(0.5\rho u^2 cs)$) to behave differently as a function of d/c (normalized ground proximity). As a result, the stable equilibrium altitudes (green dots) shift position. Note: we suspect that the peak around $d/c \sim 1.6$ in the $\theta_0 = \tau = 0$ case is due to a resonant standing wave between the hydrofoil and sidewall, so we did not report the C_L sign changes near that location to be equilibria.

small that shifting equilibria away from the ground was more difficult: after being introduced to stronger negative asymmetries ($\theta_0 \leqslant -0.5°$, $\tau \leqslant -0.2$) the equilibrium altitude disappeared (figures 5(a) and (b)). Slight negative asymmetries (e.g. $\tau = -0.1$) led to a wide range of d/c values where $C_L \approx 0$, suggesting that hydrofoils in those conditions would feel only small lateral forces over a range of altitudes.

While spatial and temporal asymmetry both shifted equilibrium altitude, they had different effects on lift, particularly very close to the ground. Introducing spatial asymmetry simply added/subtracted lift, i.e. produced a vertical shift in the $\overline{F_L}(d/c)$ curves (figure 5(a)). Introducing temporal asymmetry was more complex. Far from the ground, temporal asymmetry led to small shifts in C_L (± 0.12 when $\tau = \pm 0.3$). Near the ground, positive τ values flattened the lift curve, while negative τ values significantly amplified the lift forces. At $d/c = 0.4$, for example, a τ of $+0.3$ reduced C_L from ≈ 0.2 to ≈ -0.05, whereas a τ of -0.3 tripled C_L to ≈ 0.65. The temporal asymmetries we considered appear to have stronger, more nonlinear interactions with the ground compared to the spatial asymmetries. This is consistent with the fact that spatial asymmetry is adding linearly to the pitch function while temporal asymmetry is adding nonlinearly (equation (1)).

Our results for symmetric kinematics were also consistent with previous work in terms of thrust and efficiency. As in previous work [21, 29, 30, 44], the net thrust increased as the symmetrically pitching hydrofoil approached the wall (figures 6(a) and (b)). This 'unsteady ground effect' has been attributed to heightened added mass and circulatory forces caused by the ground [2, 14, 23, 24, 26]. The hydrodynamic power also went up near the ground (figures 6(c) and (d)), leading to a relatively constant efficiency of around 19% across all cases considered (figures 6(e) and (f)). The implication is that near-ground hydrofoils could swim at a faster speed with negligible cost in efficiency.

As they did with lift, spatial and temporal asymmetries had differing effects on thrust. Spatial asymmetries had only minor effects on thrust, power, and efficiency near the ground (figures 6(a), (c) and (e)). In contrast, temporal asymmetries increased the thrust and power coefficients significantly at all ground distances (figures 6(b) and (d)). For example, far from the ground ($d/c = 2.0$), a τ of $+0.2$ increased C_T by $\approx 15\%$, and a τ of $+0.3$ increased C_T by $\approx 28\%$. Presumably the faster pitch strokes in one direction caused a higher effective Strouhal number, leading to higher unsteady forces on the hydrofoil. Because thrust and power were affected equally, adding temporal asymmetry did not affect efficiency (figure 6(f)). The effect of the ground can be isolated by comparing the near-ground and far-from-ground cases along the same curve. For both spatial and temporal asymmetries, the thrust coefficients increased by ≈ 0.1 as the hydrofoil approached the ground, across all tested θ_0 and τ values, indicating the consistency of stand-alone propulsive benefits by swimming close to the ground.

3.2. Laterally-unconstrained experiments and simulations: equilibria can be shifted dynamically

As suggested by the tethered tests, laterally-untethered hydrofoils can adjust their equilibrium altitude in realtime by introducing pitch asymmetries. As the untethered trials started, the foils

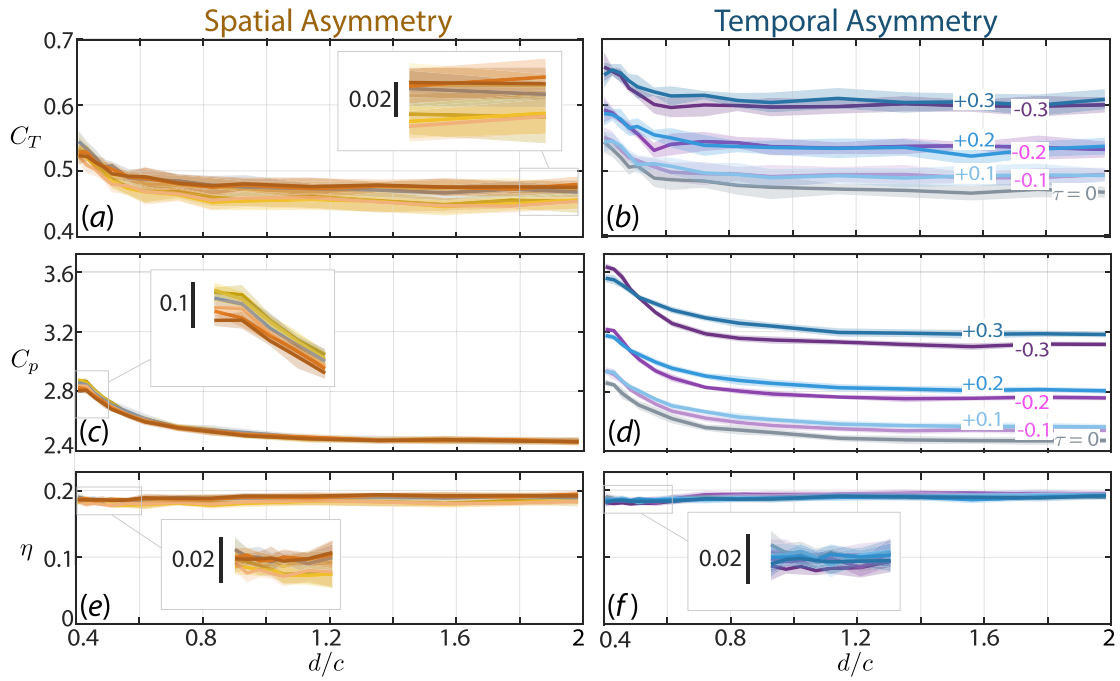

Figure 6. Thrust and power depend on both ground proximity and asymmetry. (a), (c), (e): Spatial asymmetry has little effect on thrust coefficient ($C_{F_T} \equiv \overline{T}/(0.5\rho u^2 cs)$), power coefficient ($C_p \equiv \overline{p}/(0.5\rho u^3 cs)$), or efficiency ($\eta \equiv C_T/C_p$). Curves are colored by θ_0 as in figure 5(a). (b), (d), (f): Increasing magnitude of temporal asymmetry increases thrust and power coefficients but has little effect on efficiency.

converged to the same equilibrium altitude, despite having different initial conditions (figures 7(a) and (d); Stage 1). The foils shifted to a lower equilibrium as the simulated payload (negative buoyancy) was added, a higher equilibrium as negative pitch asymmetries generated positive lift forces, then an even lower equilibrium as positive pitch asymmetries generated negative lift forces (figures 7(a) and (d); Stages 2, 3, 4).

As expected based on the tethered tests, shifting the equilibrium altitude caused noticeable changes in thrust, but not efficiency (η values within 2% of each other; figures 7(b), (c), (e) and (f)). To account for the difference in scale between the experiments and the reduced-order simulations, we reported thrust and efficiency as a percent change relative to their respective values in Stage 1 (control case; symmetric; no payload). The only significant difference between the spatial and temporal asymmetry cases was a higher percent change in thrust in Stages 3 and 4 due to the higher thrusts caused by nonzero τ values (figures 7(b) and (e)), which was consistent with what was observed in the tethered experiments (figures 6(a) and (b)).

The laterally-unconstrained hydrofoil tests do more than just validate the equilibria shifts seen in the tethered tests. While the tethered tests were quasi-steady, the untethered tests were dynamic. For example, the center of mass of the untethered hydrofoils shifted laterally within each pitch cycle, which introduced passive heaving motions and a trailing edge amplitude that were about 3 mm smaller than in the tethered case. This change in kinematics caused the absolute thrust and equilibrium altitudes to differ from those in the tethered tests. The unconstrained tests confirm that despite these changes in kinematics, the equilibria can be shifted dynamically using pitch asymmetries, as suggested by the constrained tests.

Furthermore, the potential flow simulations showed similar trends in equilibrium altitude, thrust, and efficiency. They confirmed from a theoretical perspective that near-boundary equilibria are not dominated by viscous effects. An exception appears to be the thrust in Stages 3 and 4 for temporal asymmetry, where the experiments showed a higher increase than the simulations. This difference may be the result of the dynamic boundary layer shedding that can occur around temporally asymmetric hydrofoils [45]. Such an effect would not appear in our simulations, where wake vorticity originates entirely at the trailing edge.

3.3. Fully-unconstrained simulations: equilibria are insensitive to swimming speed

Simulations of a hydrofoil that was unconstrained in both streamwise and lateral directions were used to examine the sensitivity of near-boundary equilibria to fully unconstrained free-swimming conditions. Figures 8(a) and (b) presents the simulated equilibrium altitudes for laterally unconstrained (one degree-of-freedom) and streamwise and laterally unconstrained (two degree-of-freedom) simulations

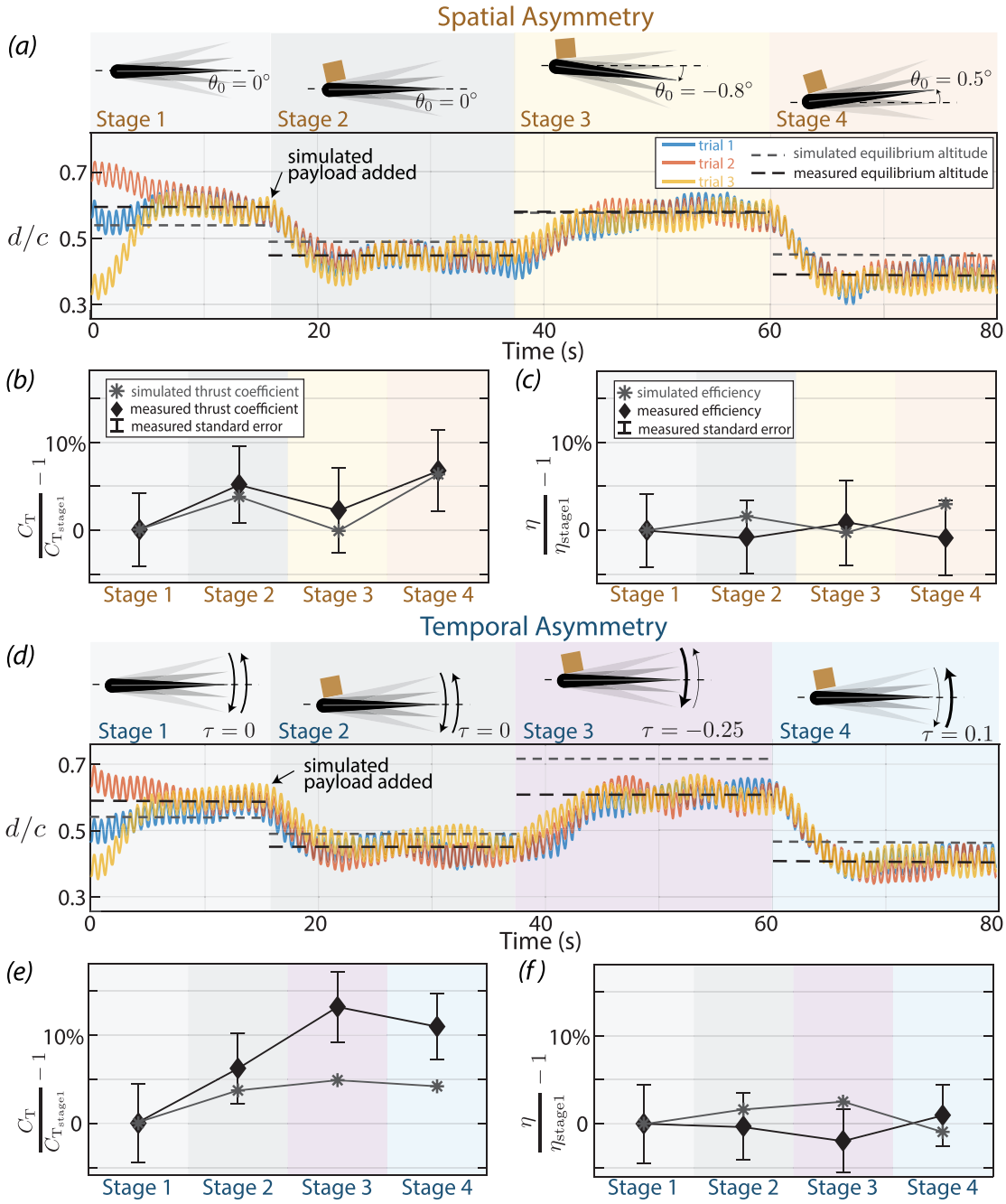

Figure 7. Untethered hydrofoil experiments and simulations confirm that asymmetric kinematics can shift equilibria. (a), (d): equilibrium altitudes are affected by both the magnitude of asymmetry and the simulated payload. (b)–(e): at later Stages, thrust increases relative to the symmetrical case (Stage 1) while no measurable changes occur in efficiency.

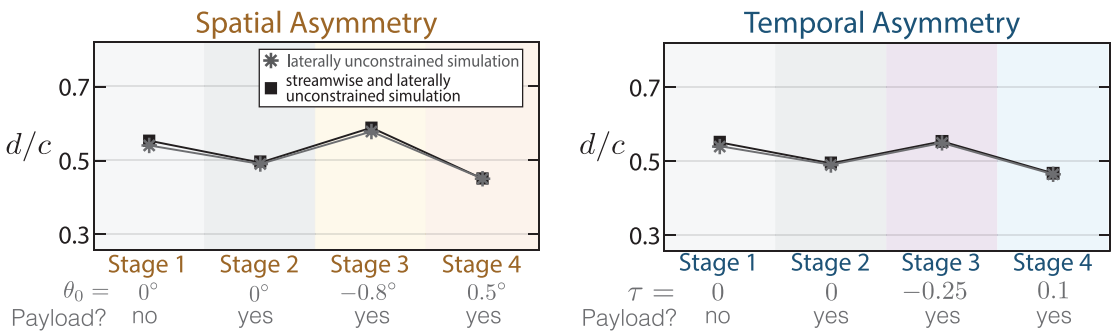

Figure 8. Insensitivity of near-boundary equilibria due to fully-unconstrained swimming conditions. (a) Equilibrium altitudes in Stages 1–4 for spatial asymmetries. (b) Equilibrium altitudes in Stages 1–4 for temporal asymmetries.

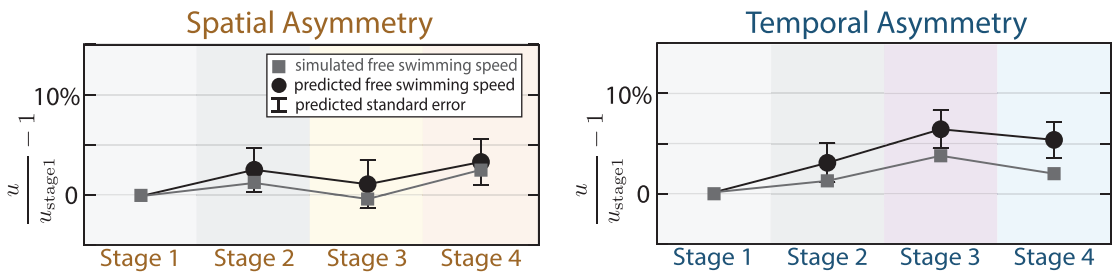

Figure 9. Percent change in simulated and predicted free swimming speeds for the fully-unconstrained simulations and laterally-unconstrained experiments, based on experimental data and scaling laws. (a) Stages 1–4 with spatial asymmetries. (b) Stages 1–4 with temporal asymmetries.

with the presences of spatial and temporal asymmetries, respectively. With streamwise freedom, the hydrofoil experienced surging oscillations due to the time-varying thrust. These surging oscillations had no significant influence on the near-boundary equilibria for both spatial and temporal asymmetries with lateral freedom. This result shows that lateral equilibria are mostly unaffected by streamwise freedom at least in inviscid flows. We postulate that this result will hold in viscous flows since experiments have shown [13] that time-averaged forces—which lead to near-boundary equilibria—are largely unaffected by surging oscillations of hydrofoils.

A clear connection between the fully-unconstrained hydrofoil simulations and the laterally-unconstrained hydrofoil experiments can be established through the free swimming speed. Employing an established inviscid scaling law for swimming speed (equation (32) in Moored and Quinn [26]), we can express the relationship between the simulated free-swimming speed and the measured laterally-unconstrained thrust coefficient as,

$$\frac{u}{u_{\text{stage1}}} - 1 = \sqrt{\frac{C_{\text{T}}}{C_{\text{Tstage1}}}} - 1, \tag{2}$$

where u_{stage1} is the free swimming speed simulated in Stage 1 of the streamwise and laterally-unconstrained simulations, C_{T} is the thrust coefficients measured during the laterally-unconstrained hydrofoil experiments (other than Stage 1), and C_{Tstage1} is the thrust coefficient in Stage 1. The speed u is the equilibrium speed for the laterally-unconstrained hydrofoil in each stage (other than Stage 1), as predicted based on the thrust measured for the constrained hydrofoil. Figure 9 presents the percent change in simulated and predicted free swimming speeds in fully-unconstrained hydrofoil simulations and laterally-unconstrained hydrofoil experiments, respectively. The predicted percent change in swimming speed is in good agreement with the streamwise and laterally-unconstrained simulations. This agreement validates that viscous effects are negligible in our setup and perhaps in dynamic ground effect more generally.

4. Discussion and conclusion

Our results demonstrate that a pitching hydrofoil's equilibrium altitude can be manipulated by using asymmetric kinematics. In many cases, the asymmetries disturb the base flow enough to shift the equilibrium; in other cases, equilibria disappear entirely. Being able to manipulate equilibrium altitudes would presumably be critical for effective near-boundary control. Cruising at the stable equilibrium altitude would require less active control, as the hydrofoil can naturally settle back into equilibrium after small disturbances, so it may be energetically-favorable to swim there. Furthermore, if the equilibrium altitude is shifted toward the ground, the hydrofoil can also benefit from higher thrust. Being able to tune the position of near-boundary equilibria may therefore be a useful feature of near-boundary locomotion.

In addition to the thrust benefits, shifting equilibrium altitudes toward the ground may also increase stability. The slope of the $C_{\text{L}}(d/c)$ curves at equilibrium is a key feature of near-boundary dynamics because of its implications for stability. If, for example, lift were defined via the derivative of some force potential U ($F_{\text{L}} \equiv -\text{d}U/\text{d}d$), then steeper slopes in the lift curve ($F_{\text{L}}(d)$) would imply narrower local minima in the force potential ($U(d)$). As a result, higher values of the lift slope at equilibrium would theoretically increase lateral stability, and stronger perturbations would be required to break free from these equilibrium altitudes. The slope of the $C_{\text{L}}(d/c)$ curves at equilibrium altitude increases for both spatial (figure 5(a) $\theta_0 = 0°, +0.5°, +1.0°$) and temporal asymmetries (figure 5(b) $\tau = 0, +0.1, +0.2$). As the slope steepens, the hydrofoil feels a stronger upward push just below equilibrium and a stronger downward push just above equilibrium. In this way, pitch asymmetries could in theory be used to stabilize a hydrofoil's proximity to a solid boundary. Note that if potential flow is assumed, a near-boundary hydrofoil has the same boundary conditions as two side-by-side hydrofoils pitching out of phase [10], so it is possible that asymmetries could also help

tune the separation and stability of two side-by-side swimmers.

Consider, for example, how these implications apply to real near-boundary swimmers and flyers. Elasmobranchs, which include bottom-dwelling rays, tend to be negatively buoyant [39]. In light of our findings, it may be that negative-buoyancy is—at some altitude—counteracted by an upward lift force, leading to a stable equilibrium altitude closer to the ground (as in figure 7, Stage 2). A ray could employ asymmetric kinematics to further shift this equilibrium altitude either closer to or away from the ground at will. For example, cownose rays are known to use a larger upstroke than downstroke (spatial asymmetry) [33, 43]. The role of near-boundary lateral forces may even help to explain some of the kinematic and morphological differences that are known to exist between pelagic (open-water) and benthic (bottom-dwelling) aquatic animals [8, 32]. For example, the fact that temporal asymmetry provides thrust benefits independent of ground distance may help explain why mid-ocean swimmers, like dolphins [35, 38], tend to employ temporal asymmetry (faster downstrokes than upstrokes) as supposed to spatial asymmetry.

Regardless of their biological implications, our results offer some concrete control strategies for near-boundary bio-inspired propulsors. It appears that both spatial and temporal asymmetries can be used to manipulate equilibrium altitude and near-boundary stability (figure 7). This finding suggests that bio-inspired vehicles with fin-like propulsors could use either strategy to fine-tune their equilibrium altitude near a boundary. The chosen asymmetry type would likely depend on hardware constraints. For example, a servo-driven fin might use a constant pitch offset to achieve spatial asymmetry, whereas a fin actuated with a scotch-yoke mechanism might use sawtooth motor commands to achieve temporal asymmetry. We hypothesize that these equilibria-manipulation strategies could offer propulsive benefits if incorporated into bio-inspired robots that swim/fly near boundaries. Particularly when combined with artificial intelligence techniques like deep learning, these strategies could potentially help vehicles stay more efficient and stable when operating near solid boundaries.

Data availability statement

The data that support the findings of this study are openly available at the following URL/DOI: https://drive.google.com/drive/folders/1asYUJ3p7ZG2ZVL4VJbN-ucS53Xo2RMr0?usp=sharing. Data will be available from 29 July 2022.

Acknowledgments

This work was made possible by funding from the National Science Foundation (PI Daniel B Quinn and Keith W Moored; Award Nos. 1921809, 2040351, 1829004, and 1653181; Program Managers: Dr Ron Joslin and Dr Francesmary Modugno).

ORCID iDs

Leo Liu https://orcid.org/0000-0002-6488-6782
Qiang Zhong https://orcid.org/0000-0002-8435-5938
Tianjun Han https://orcid.org/0000-0002-5319-123X
Keith W Moored https://orcid.org/0000-0002-4331-3774
Daniel B Quinn https://orcid.org/0000-0002-5835-5221

References

[1] Anderson E, McGillis W and Grosenbaugh M 2001 The boundary layer of swimming fish *J. Exp. Biol.* **204** 81–102
[2] Ayancik F, Zhong Q, Quinn D, Brandes A, Bart-Smith H and Moored K 2019 Scaling laws for the propulsive performance of three-dimensional pitching propulsors *J. Fluid Mech.* **871** 1117–38
[3] Baudinette R V and Schmidt-Nielsen K 1974 Energy cost of gliding flight in herring gulls *Nature* **248** 83–84
[4] Bergstad O 2009 Fish: demersal fish (life histories, behavior, adaptations) *Elements of Physical Oceanography: A Derivative of the Encyclopedia of Ocean Sciences* vol 363 (London: Academic Press)
[5] Blake R 1983 Mechanics of gliding in birds with special reference to the influence of the ground effect *J. Biomech.* **16** 649–54
[6] Blake R W 1979 The energetics of hovering in the mandarin fish (Synchropus picturatus) *J. Exp. Biol.* **82** 25–33
[7] Blevins E L and Lauder G V 2013 Swimming near the substrate: a simple robotic model of stingray locomotion *Bioinspir. Biomim.* **8** 016005
[8] Cooper W J, Carter C B, Conith A J, Rice A N and Westneat M W 2017 The evolution of jaw protrusion mechanics is tightly coupled to bentho-pelagic divergence in damselfishes (Pomacentridae) *J. Exp. Biol.* **220** 652–66
[9] Dai L, He G and Zhang X 2015 Self-propulsion of a flexible plunging foil near a solid wall *Proc. Eng.* **126** 431–5
[10] Dewey P A, Quinn D B, Boschitsch B M and Smits A J 2014 Propulsive performance of unsteady tandem hydrofoils in a side-by-side configuration *Phys. Fluids* **26** 041903
[11] Eloy C 2012 Optimal Strouhal number for swimming animals *J. Fluids Struct.* **30** 205–18
[12] Fernandez-Prats R, Raspa V, Thiria B, Huera-Huarte F and Godoy-Diana R 2015 Large-amplitude undulatory swimming near a wall *Bioinspir. Biomim.* **10** 016003
[13] Floryan D, Buren T V and Smits A J 2018 Efficient cruising for swimming and flying animals is dictated by fluid drag *Proc. Natl Acad. Sci. USA* **115** 8116–8
[14] Floryan D, Van Buren T, Rowley C W and Smits A J 2017 Scaling the propulsive performance of heaving and pitching foils *J. Fluid Mech.* **822** 386–97

[15] HAINSWORTH F R 1988 Induced drag savings from ground effect and formation flight in brown pelicans *J. Exp. Biol.* **135** 431–44
[16] Hedrick T L, Cheng B and Deng X 2009 Wingbeat time and the scaling of passive rotational damping in flapping flight *Science* **324** 252–5
[17] Johansson L C, Jakobsen L and Hedenström A 2018 Flight in ground effect dramatically reduces aerodynamic costs in bats *Curr. Biol.* **28** 3502–7.e4
[18] Katz J 1985 Calculation of the aerodynamic forces on automotive lifting surfaces. *Trans. ASME, J. Fluids Eng.* **107** 438–43
[19] Katz J and Plotkin A 2005 *Low Speed Aerodynamics. From Wing Theory to Panel Methods* vol 632 (Cambridge: Cambridge University Press)
[20] Krasny R 1986 Desingularization of periodic vortex sheet roll-up *J. Comput. Phys.* **65** 292–313
[21] Kurt M, Cochran-Carney J, Zhong Q, Mivehchi A, Quinn D and Moored K 2019 Swimming freely near the ground leads to flow-mediated equilibrium altitudes *J. Fluid Mech.* **875** 1–14
[22] Lauder G V 2015 Fish locomotion: recent advances and new directions *Annu. Rev. Mar. Sci.* **7** 521–45
[23] Mivehchi A, Dahl J and Licht S 2016 Heaving and pitching oscillating foil propulsion in ground effect *J. Fluids Struct.* **63** 174–87
[24] Mivehchi A, Zhong Q, Kurt M, Quinn D B and Moored K W 2021 Scaling laws for the propulsive performance of a purely pitching foil in ground effect *J. Fluid Mech.* **919** R1
[25] Moored K W 2018 Unsteady three-dimensional boundary element method for self-propelled bio-inspired locomotion *Comput. Fluids* **167** 324–40
[26] Moored K W and Quinn D B 2019 Inviscid scaling laws of a self-propelled pitching airfoil *AIAA J.* **57** 3686–700
[27] Park H and Choi H 2010 Aerodynamic characteristics of flying fish in gliding flight *J. Exp. Biol.* **213** 3269–79
[28] Park S G, Kim B and Sung H J 2017 Hydrodynamics of a self-propelled flexible fin near the ground *Phys. Fluids* **29** 051902
[29] Quinn D B, Moored K W, Dewey P A and Smits A J 2014 Unsteady propulsion near a solid boundary *J. Fluid Mech.* **742** 152–70
[30] Quinn D, Lauder G and Smits A 2014 Flexible propulsors in ground effect *Bioinspir. Biomim.* **9** 036008
[31] Rayner J M V 1991 On the aerodynamics of animal flight in ground effect *Phil. Trans. R. Soc.* B **334** 119–28
[32] Rosenberger L J 2001 Pectoral fin locomotion in batoid fishes: undulation versus oscillation *J. Exp. Biol.* **204** 379–94
[33] Russo R, Blemker S, Fish F and Bart-Smith H 2015 Biomechanical model of batoid (skates and rays) pectoral fins predicts the influence of skeletal structure on fin kinematics: implications for bio-inspired design *Bioinspir. Biomim.* **10** 046002
[34] Spedding G, Rayner J and Pennycuick C 1984 Momentum and energy in the wake of a pigeon (Columba livia) in slow flight *J. Exp. Biol.* **111** 81–102
[35] Tanaka H, Li G, Uchida Y, Nakamura M, Ikeda T and Liu H 2019 Measurement of time-varying kinematics of a dolphin in burst accelerating swimming *PLoS One* **14** 1–25
[36] Tang C, Huang H, Gao P and Lu X 2016 Self-propulsion of a flapping flexible plate near the ground *Phys. Rev.* E **94** 033113
[37] Taylor G K, Nudds R L and Thomas A L R 2003 Flying and swimming animals cruise at a Strouhal number tuned for high power efficiency *Nature* **425** 707–11
[38] Videler J and Kamermans P 1985 Differences between upstroke and downstroke in swimming dolphins *J. Exp. Biol.* **119** 265–74
[39] Webb P W 1994 The biology of fish swimming *Mechanics and Physiology of Animal Swimming* vol 4562 (Cambridge: Cambridge University Press)
[40] Withers P and Timko P 1977 The significance of ground effect to the aerodynamic cost of flight and energetics of the black skimmer (Rhyncops nigra) *J. Exp. Biol.* **70** 13–26
[41] Wu X, Zhang X, Tian X, Li X and Lu W 2020 A review on fluid dynamics of flapping foils *Ocean Eng.* **195** 106712
[42] Zhang C, Huang H and Lu X-Y 2017 Free locomotion of a flexible plate near the ground *Phys. Fluids* **29** 041903
[43] Zheng L, Bi S, Cai Y and Niu C 2010 Design and optimization of a robotic fish mimicking cow-nosed ray *2010 IEEE Int. Conf. on Robotics and Biomimetics* (IEEE) pp 1075–80
[44] Zhong Q, Han T, Moored K W and Quinn D B 2021 Aspect ratio affects the equilibrium altitude of near-ground swimmers *J. Fluid Mech.* **917** A36
[45] Zhong Q and Quinn D 2021 Streamwise and lateral maneuvers of a fish-inspired hydrofoil *Bioinspir. Biomim.* **16** 056015
[46] Zhu Q, Wolfgang M J, Yue D K P and Triantafyllou M S 2002 Three-dimensional flow structures and vorticity control in fish-like swimming *J. Fluid Mech.* **468** 1–28